



Quantum computing quantum Monte Carlo with hybrid tensor network for electronic structure calculations



Shu Kanno ^{1,2}✉, Hajime Nakamura ^{2,3}, Takao Kobayashi ^{1,2}, Shigeki Gicho ^{2,4}, Miho Hatanaka ^{2,4}, Naoki Yamamoto ^{2,5} & Qi Gao ^{1,2}

Quantum computers have a potential for solving quantum chemistry problems with higher accuracy than classical computers. Quantum computing quantum Monte Carlo (QC-QMC) is a QMC with a trial state prepared in quantum circuit, which is employed to obtain the ground state with higher accuracy than QMC alone. We propose an algorithm combining QC-QMC with a hybrid tensor network to extend the applicability of QC-QMC beyond a single quantum device size. In a two-layer quantum-quantum tree tensor, our algorithm for the larger trial wave function can be executed than preparable wave function in a device. Our algorithm is evaluated on the Heisenberg chain model, graphite-based Hubbard model, hydrogen plane model, and MonoArylBilimidazole using full configuration interaction QMC. Our algorithm can achieve energy accuracy (specifically, variance) several orders of magnitude higher than QMC, and the hybrid tensor version of QMC gives the same energy accuracy as QC-QMC when the system is appropriately decomposed. Moreover, we develop a pseudo-Hadamard test technique that enables efficient overlap calculations between a trial wave function and an orthonormal basis state. In a real device experiment by using the technique, we obtained almost the same accuracy as the statevector simulator, indicating the noise robustness of our algorithm. These results suggests that the present approach will pave the way to electronic structure calculation for large systems with high accuracy on current quantum devices.

Computationally accurate prediction of physical properties can accelerate the development of functional materials such as batteries^{1,2}, catalysis³, and photochemical materials^{4,5}. The physical properties are mainly governed by the electrons in the materials, and the computational cost of calculating electronic structures increases exponentially with system size in general, which often prevents classical computers from achieving the required accuracy to predict the properties.

Quantum computers are expected to solve such classically intractable problems in quantum chemistry and materials science⁶. Current quantum computers, called noisy intermediate scale-quantum (NISQ) devices⁷, have limitations on the numbers of qubits and quantum gates due to physical noise, and various approaches for the NISQ devices have been proposed^{8,9}. One of the most popular algorithms is the variational quantum eigensolver (VQE)¹⁰, which is used to obtain the ground state energy by

minimizing energy cost function using a variational quantum circuit, where its parameters are updated by a classical computer. Contrary to the traditional quantum algorithms such as the quantum phase estimation¹¹, VQE requires reduced hardware resources. However, VQE suffers from many issues such as insufficient accuracy¹² and vanishing parameter gradients, so-called barren plateau¹³.

In addition to studies to avoid those issues^{14–17}, there are multiple variants of quantum Monte Carlo (QMC), which were proposed for further relaxing the hardware requirements^{18–24}. QMC is a computational method using stochastic sampling techniques to solve large quantum many-body problems such as molecular systems containing hundreds of electrons^{25,26}. To date, various types of QMC approaches have been proposed, including variational Monte Carlo^{27,28}, auxiliary field quantum Monte Carlo^{29,30}, and full configuration interaction quantum Monte Carlo (FCIQMC)³¹. In this study, we adopt FCIQMC, which is useful for quantum chemistry, a

¹Mitsubishi Chemical Corporation, Science & Innovation Center, Yokohama 227-8502, Japan. ²Quantum Computing Center, Keio University, Yokohama 223-8522, Japan. ³IBM Quantum - IBM Research Tokyo, Tokyo 103-8510, Japan. ⁴School of Fundamental Science and Technology, Faculty of Science and Technology, Keio University, Yokohama 223-8522, Japan. ⁵Department of Applied Physics and Physico-Informatics, Keio University, 3-14-1 Hiyoshi, Kohoku-ku, Yokohama 223-8522, Japan. ✉e-mail: shu.kanno@quantum.keio.ac.jp

stochastic imaginary-time evolution is executed in the space of all the orthonormal basis states (such as the Slater determinants) that can be constructed from a given spatial orbital basis. As in refs. 18,21,22, a type of QMC called quantum computing QMC (QC-QMC) was introduced. Combined with a quantum algorithm such as VQE, QC-QMC can improve the energy evaluation accuracy in ground-state calculations. Specifically, the wave function distribution, i.e., the walker distribution, is generated on a classical²¹ (or quantum^{18,22}) device, and energy is evaluated by using a trial wave function prepared by VQE. Contrary to VQE where the accuracy depends on parameter optimization, QC-QMC has no such optimization and the accuracy relies on the quality of the trial wave functions, the algorithms, and calculation settings in the energy evaluation. Avoiding strict VQE optimizations lowers the hardware requirements; for example, there was a demonstration on a diamond model constructed in 16 qubits, the largest hardware experiment run nearly within the chemical accuracy (chemical precision)¹⁸.

While QC-QMC can provide highly accurate ground-state calculations, applying this method to large-scale systems is challenging. Although the electronic correlations outside the active space can be obtained by classical post-processing¹⁸, the available active space size^{32,33} is limited by the size of the trial wave function i.e., the number of qubits. The proposals for constructing wave functions larger than the quantum device size include the divide-and-conquer algorithm^{34,35}, embedding theory^{36–38}, circuit cutting^{39,40}, perturbation⁴¹, and tensor network^{42,43}. Hybrid tensor network (HTN)⁴³ is a general tensor network framework that can be implemented on a reduced number of qubits and gates by decomposing the wave function in the original system into smaller-sized tensors. These tensors are processed by quantum or classical computation, i.e., quantum/classical hybrid computation. Such a decomposition can reduce the effective width and depth of the circuit, making it more robust to noise than the original circuit. There are several quantum algorithms or ansatze depending on the tensor network structure, including the matrix product states⁴⁴, projected entangled pair states⁴⁵, and tree tensor networks (TN)^{42,46}. In the two-layer TN adopted in this study, the quantum states of the subsystem in the first layer are integrated with the second layer by using a quantum or classical method, referred to as the quantum-quantum TN (QQTN) and quantum-classical TN, respectively. The deep VQE³⁵ and entanglement forging^{47,48} can be broadly classified into the quantum-quantum and quantum-classical ones, respectively. If gaining the quantum advantage (rather than noise robustness) is a priority, QQTN is preferred.

In this study, we propose an algorithm of QC-QMC in combination with HTN of a two-layered QQTN. In particular, we consider the following QQTN:

$$\begin{aligned} & |\psi_{\text{HTN}}(\vec{\theta}_{\text{HTN}})\rangle \\ &= \sum_{\vec{i}} \psi_{\vec{i}}(\vec{\theta}_U) \left(\prod_{m=1}^k \sum_{\vec{j}_m} \varphi_{\vec{j}_m}^{i_m}(\vec{\theta}_{Lm}) \right) \left(\bigotimes_{m=1}^k |\vec{j}_m\rangle \right) \quad (1) \\ &= \sum_{\vec{i}} \psi_{\vec{i}}(\vec{\theta}_U) \bigotimes_{m=1}^k |\varphi_{\vec{j}_m}^{i_m}(\vec{\theta}_{Lm})\rangle. \end{aligned}$$

The tensor network representation of this state is depicted in Fig. 1a. The tensors $\psi_{\vec{i}}(\vec{\theta}_U)$ ($\varphi_{\vec{j}_m}^{i_m}(\vec{\theta}_{Lm})$) are defined using wave functions $|\psi\rangle$ ($|\varphi\rangle$) and $\langle\psi|\psi\rangle$ ($\langle\varphi|\varphi\rangle$) as $\psi_{\vec{i}}(\vec{\theta}_U) = \langle\vec{i}|\psi(\vec{\theta}_U)\rangle$ ($\varphi_{\vec{j}_m}^{i_m}(\vec{\theta}_{Lm}) = \langle\vec{j}_m|\varphi(\vec{\theta}_{Lm})\rangle$), where $\vec{i} = i_1 i_2 \dots i_k$ ($\vec{j}_m = j_{m1} j_{m2} \dots j_{mn}$) represent a k (n)-qubit binary string, and the subscript \vec{j}_m of $\varphi_{\vec{j}_m}^{i_m}(\vec{\theta}_{Lm})$ is omitted in Fig. 1. $\psi_{\vec{i}}(\vec{\theta}_U)$ and $\varphi_{\vec{j}_m}^{i_m}(\vec{\theta}_{Lm})$ are assumed to be constructed by quantum circuits, where $\vec{\theta}_U$ and $\vec{\theta}_{Lm}$ are variational parameters of the upper tensor (blue) and the m -th lower tensor (orange), respectively. The subscripts U and L designate the upper and lower

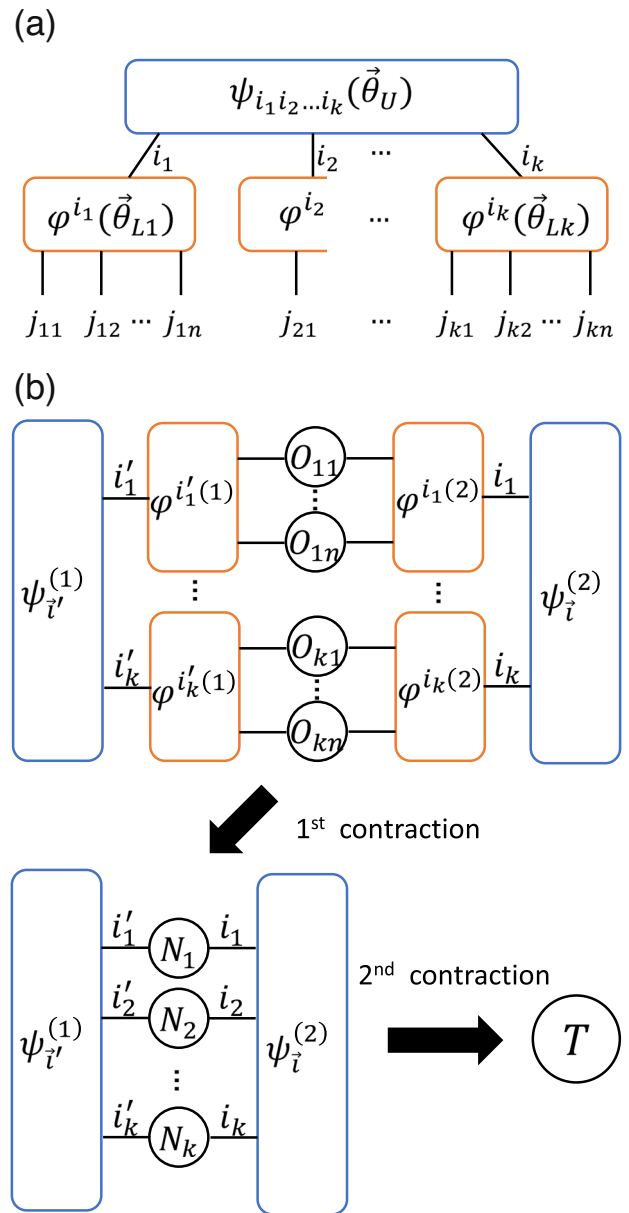


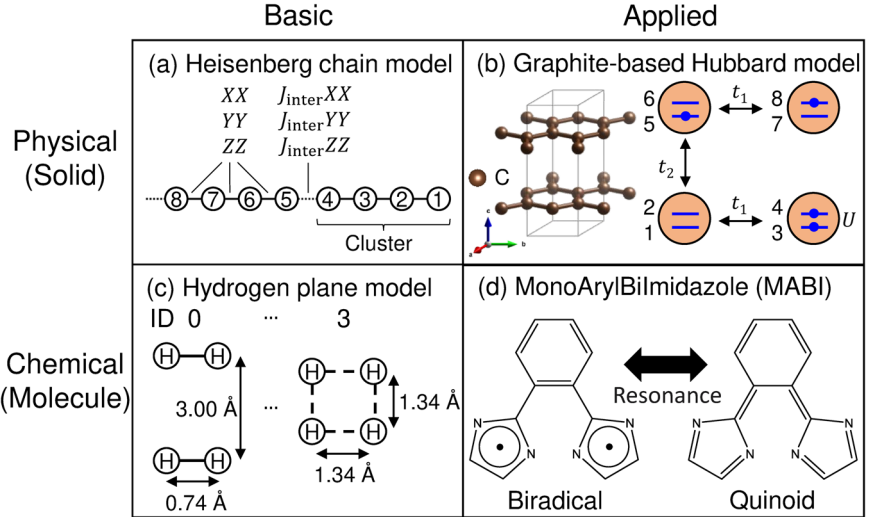
Fig. 1 | Representation and calculation of hybrid tensor network in the two-layer QQTN. **a** Hybrid tensor network representation of the two-layered QQTN state. **b** Calculation of T in Eq. (2), where we omit the parameters. See Section IV C for details.

tensors, respectively. k and nk represent the number of subsystems and system qubits, respectively. The algorithm details are given in Section IV (and Supplementary Informations 1, 2, and 3), where calculating the transition amplitude between a pair of the wave functions $T(\vec{\theta}_{\text{HTN}}^{(1)}, \vec{\theta}_{\text{HTN}}^{(2)})$ is a major part:

$$T(\vec{\theta}_{\text{HTN}}^{(1)}, \vec{\theta}_{\text{HTN}}^{(2)}) = \langle \psi_{\text{HTN}}^{(1)}(\vec{\theta}_{\text{HTN}}^{(1)}) | O | \psi_{\text{HTN}}^{(2)}(\vec{\theta}_{\text{HTN}}^{(2)}) \rangle, \quad (2)$$

where the observable O is defined using tensor products $O = \bigotimes_{m,r} O_{mr}$ and O_{mr} is an observable attached on the r -th qubit of the m -th subsystem ($r = 1, 2, \dots, n$). As shown in Fig. 1b, the transition amplitude $T(\vec{\theta}_{\text{HTN}}^{(1)}, \vec{\theta}_{\text{HTN}}^{(2)})$ is calculated by performing a quantum computation on the lower tensor, classically processing the obtained results to generate the

Fig. 2 | Models for benchmarking HTN+QMC. The structure of graphite is drawn by VESTA²². The qubit indices are labeled in **a, b** (see Section II A for details). **a** Heisenberg chain model. **b** Graphite-based Hubbard model. **c** Hydrogen plane model. **d** MonoArylBilimidazole (MABI).



contracted operators N_m and then contracting with a quantum computation on the upper tensor. Substituting $|\psi_{\text{HTN}}^{(1)}(\vec{\theta}_{\text{HTN}}^{(1)})\rangle = |\psi_{\text{HTN}}^{(2)}(\vec{\theta}_{\text{HTN}}^{(2)})\rangle = |\psi_{\text{HTN}}(\vec{\theta}_{\text{HTN}})\rangle$ in Eq. (2) yields the estimation of the observable

$$\langle \psi_{\text{HTN}}(\vec{\theta}_{\text{HTN}}) | O | \psi_{\text{HTN}}(\vec{\theta}_{\text{HTN}}) \rangle, \quad (3)$$

and by substituting $|\psi_{\text{HTN}}^{(1)}(\vec{\theta}_{\text{HTN}}^{(1)})\rangle = |\psi_{\text{HTN}}(\vec{\theta}_{\text{HTN}})\rangle$, $|\psi_{\text{HTN}}^{(2)}(\vec{\theta}_{\text{HTN}}^{(2)})\rangle = |\phi_h\rangle$, and $O = I^{\otimes nk}$ in Eq. (2), we obtain the overlap with the h -th orthonormal basis state $|\phi_h\rangle$ (e.g., the Slater determinant)

$$\langle \psi_{\text{HTN}}(\vec{\theta}_{\text{HTN}}) | \phi_h \rangle. \quad (4)$$

The HTN+QMC algorithm consists of two steps: first, we optimize $\vec{\theta}_{\text{HTN}} = (\vec{\theta}_U, \vec{\theta}_{Lm})$ to prepare the trial wave function, by calculating Eq. (3). Second, we execute QMC by using the trial wave function $|\psi_{\text{HTN}}(\vec{\theta}_{\text{HTN}})\rangle$, which was optimized in the first step, and using Eq. (4). We will denote HTN+VQE when referring to the first step only and omit the parameter in $|\psi_{\text{HTN}}\rangle$ hereafter. In this formalism, by using the contraction technique shown in Fig. 1b, we can construct a nk qubit tree-type trial wave function in QMC by using a n qubit device with a linear measurement overhead. Note that the dimension of the subsystem represented by each lower tensor is determined by the number of the legs connected to the upper tensor. Under such restrictions, therefore, how to decompose the target system into the subsystems is a crucial factor in achieving a high fidelity of the tensor product state.

We benchmarked the performance of our algorithm for the Heisenberg chain model, hydrogen (H_4) plane model, graphite-based Hubbard model, and MonoArylBilimidazole (MABI), which are classified into four material categories: physical or chemical (solid or molecule) and basic or applied as in Fig. 2. The first two models are commonly used as the benchmark model^{18,49}. Graphite is a two-dimensional layered material and is used as an anode in lithium-ion batteries⁵⁰. MABI is a model system of the photochromic radical dimer PentaArylBiImidazole (PABI)⁵¹. We also execute on a real device *ibmq_kolkata* by developing a technique to calculate the overlap between the trial wave function and orthonormal basis state required in HTN+QMC. We call this technique a pseudo-Hadamard

test because the Hadamard test type circuit is used in the technique. We mention that the proposed algorithm can be applied to other HTN structures and QMC types. For example, by changing the overlap calculation in the original QC-AFQMC¹⁸ to the calculation introduced in this paper, it could be extended to the HTN version.

Finally, while our main objective is to large-scale QC-QMC by using HTN, we should comment on the treatment of the sign problem in this study. In previous research on QC-QMC^{18,21,22}, there are two steps where quantum computation is utilized: one related to walker control, and the other (projected) energy evaluation. Both steps employ quantum computation for overlap or transition amplitude calculations. In this study, we adopted a method that applies quantum computation only to the energy calculation²¹. While this method reduces the variance of energy evaluation, it does not essentially address the sign problem of FCIQMC, where the required number of walkers exponentially increases with system size. To tackle the problem, we should address the method related to a walker control, for example, the construction of an orthonormal basis using a unitary transformation by VQE²², in which the QMC wave function is represented more sparsely than in the Slater determinant basis. In Supplementary Information 4, we provide an overview of the HTN+FCIQMC algorithm including the sparse basis construction. However, this algorithm was not tested in this study due to its high computational cost for verifications and the fact that it is far from the main purpose of this study, which is to extend QC-QMC to HTN.

Results

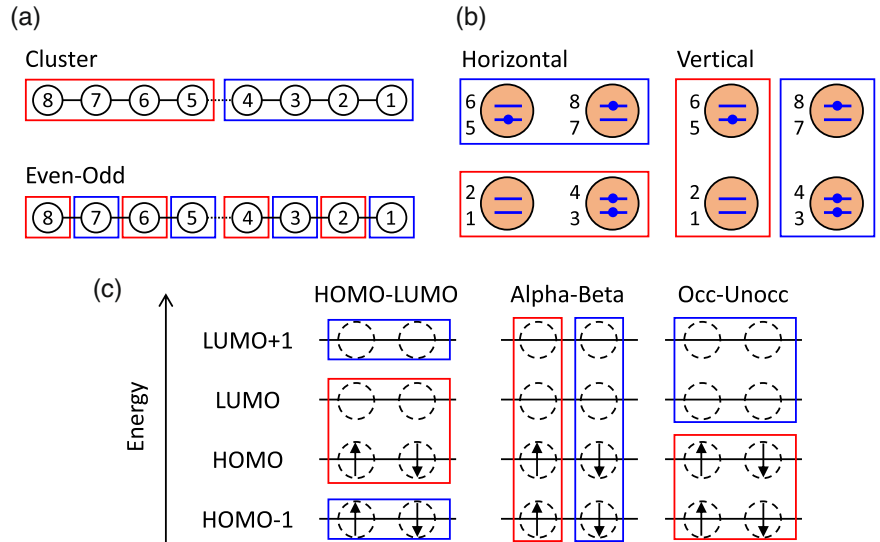
We first explain the benchmarking models. Next, we demonstrate the performance in HTN+QMC for the Heisenberg chain model, followed by the analysis of all the benchmarking models. Then, we describe the operational principle of the pseudo-Hadamard test technique and present the corresponding results of the real device experiments for the hydrogen plane model and MABI.

Benchmarking models

The performance of HTN+QMC is benchmarked with the Heisenberg chain model, graphite-based Hubbard model, hydrogen plane model, and MABI. The Heisenberg chain model, as shown in Fig. 2a, is defined as a chain of k clusters consisting of four sites

$$H = \sum_{p=1}^k H_p + J_{\text{inter}} \sum_{p'=1}^{k-1} H_{p'}, \quad (5)$$

Fig. 3 | Decomposition settings. $n = 4$ and $k = 2$ are assumed for all the models in this figure.
a Heisenberg chain model. **b** Graphite-based Hubbard model. **c** Chemical models in the case of the eight-qubit model.



where

$$H_p = \sum_{f=1}^3 X_{4(p-1)+f} X_{4(p-1)+f+1} + Y_{4(p-1)+f} Y_{4(p-1)+f+1} + Z_{4(p-1)+f} Z_{4(p-1)+f+1}, \quad (6)$$

$$H_{p'} = X_{4p'} X_{4p'+1} + Y_{4p'} Y_{4p'+1} + Z_{4p'} Z_{4p'+1}. \quad (7)$$

The intra- and inter-cluster interactions are 1 and J_{inter} , respectively. In the benchmark, we consider $k = 2$ and 3, i.e., 8- and 12-qubit models and $J_{\text{inter}} = 0.2, 0.4, \dots, 2.0$. We assume that the J_{inter} is described by atomic unit (i.e., Hartree), but except when necessary, the unit is omitted according to convention.

Figure 2b shows our graphite-based Hubbard model (the graphite model hereafter), where two layers of graphene sheets are modeled with periodically aligned unit cells, in which two carbon atoms reside in each layer. Using two qubits to represent the up and down spin orbitals (p_z orbitals) in each carbon atom, we define the Hamiltonian with 8 qubits as

$$H = 3t_1 \sum_{q=1,2,5,6} (a_{q+2}^\dagger a_q + a_q^\dagger a_{q+2}) + 2t_2 \sum_{q=1,2} (a_{q+4}^\dagger a_q + a_q^\dagger a_{q+4}) + U \sum_{q=1,3,5,7} n_{q+1} n_q, \quad (8)$$

where q is the spin-orbital index for the p_z orbital in carbon, and $q = 1, 2, 3$, and 4 (5, 6, 7, and 8) corresponds to the first (second) layer. a_q^\dagger (a_q) is the creation (annihilation) operators on the q -th site and n_q is the number operator $n_q = a_q^\dagger a_q$. t_1 and t_2 are the hopping energy between the first and second nearest neighbor sites corresponding to the intra- and inter-layer interaction energy, respectively, and U is the on-site Coulomb energy. The prefactors for t_1 and t_2 arise from periodic boundary conditions, e.g., the prefactor for t_2 is 2 because two inter-layer interactions exist per carbon (one inside and the other outside the unit cell). The reason for t_2 being only on two indices, $q = 1$ and 2, is because graphite is AB stacking. We determine the value of t_1 , t_2 , and U using the electronic structure calculation. See Supplementary Information 5 for details.

The Hamiltonians for the hydrogen plane model (8-qubit model) in Fig. 2c and MABI (12-qubit model) in Fig. 2d were constructed using their restricted Hartree-Fock orbitals of their ground states as molecular orbital bases. In the hydrogen plane model, the two hydrogen molecules are arranged vertically as in the index (ID) 0 of Fig. 2c. Then, the intermolecular

and intramolecular distances are shortened and lengthened, respectively, until the hydrogen plane becomes a square as in ID 3. The two structures are interpolated between ID 0 and 3, benchmarking four structures.

Next, we present the specific conditions for constructing the benchmarking models. The decomposition settings used for individual models are as follows: for the Heisenberg chain model, the cluster and even-odd settings refer to decomposing the model into subsystems by the cluster and even-odd indices, respectively, as illustrated in Fig. 3a; for the graphite model, the horizontal and vertical settings refer to decomposing the model horizontally and vertically with respect to the sheet (in the ab-axis plane in Fig. 2b), respectively, as in Fig. 3b; for the chemical models (hydrogen plane model and MABI), the HOMO-LUMO, alpha-beta, and occ-unocc settings refer to decomposing the model using the pair of HOMO $- x$ and LUMO $+ x$ as units ($x = 0$ and 1 in the hydrogen plane model and $x = 0, 1$, and 2 in MABI), based on alpha and beta spin-orbitals, as well as occupied and unoccupied orbitals, respectively, as in Fig. 3c, where the orbitals of the chemical models are shown in Supplementary Information 5; the no-decomposition setting refers to the calculation without decomposing the original system, i.e., not using HTN. The cluster setting for the Heisenberg model, the horizontal setting for the graphite model, and the HOMO-LUMO setting for chemical models are adopted as a default.

Figure 4 shows the quantum circuit called real amplitude ansatz, a popular hardware efficient ansatz employed for devices with linear connectivity layout, where d_H , d_N , and \tilde{d}_H denote the depth in HTN, the no-decomposition setting, and HTN used for real device, i.e., the block surrounded by the dotted line is repeated d_H or d_N , and \tilde{d}_H times, respectively. Figure 4a shows the original circuit, which is used for the statevector simulation, whereas, in order to run on real devices, a variant with ancilla qubit was considered, as in Fig. 4b; details on the operation are given in Section II C. In both ansatze, the rotation angle of the RY gate (i.e., the parameter) is updated at VQE and HTN+VQE iterations, while in the second step of QC-QMC and HTN+QMC, it is fixed. Because HTN+VQE demands quite a high computational cost due to its iterative process, the real device (*ibmq_kolkata*) was used only for the overlap calculation in the second step, i.e., not for HTN+VQE computations.

The depth represents a value for the real amplitude ansatze, which are k -qubit and n -qubit circuits for upper and lower tensors, respectively, in HTN, whereas nk -qubit circuits in the no-decomposition setting (in which ancilla qubit is not counted). Thus, the numbers of parameters in the HTN and no-decomposition settings are different even with $d_H = d_N$, whereas the numbers in the statevector and real device procedure of HTN are the same when $d_H = \tilde{d}_H$. The numbers of parameters in the HTN settings with d_H and the no-decomposition setting with d_N are $nk(d_H + 1) + k(d_H + 1)$ and

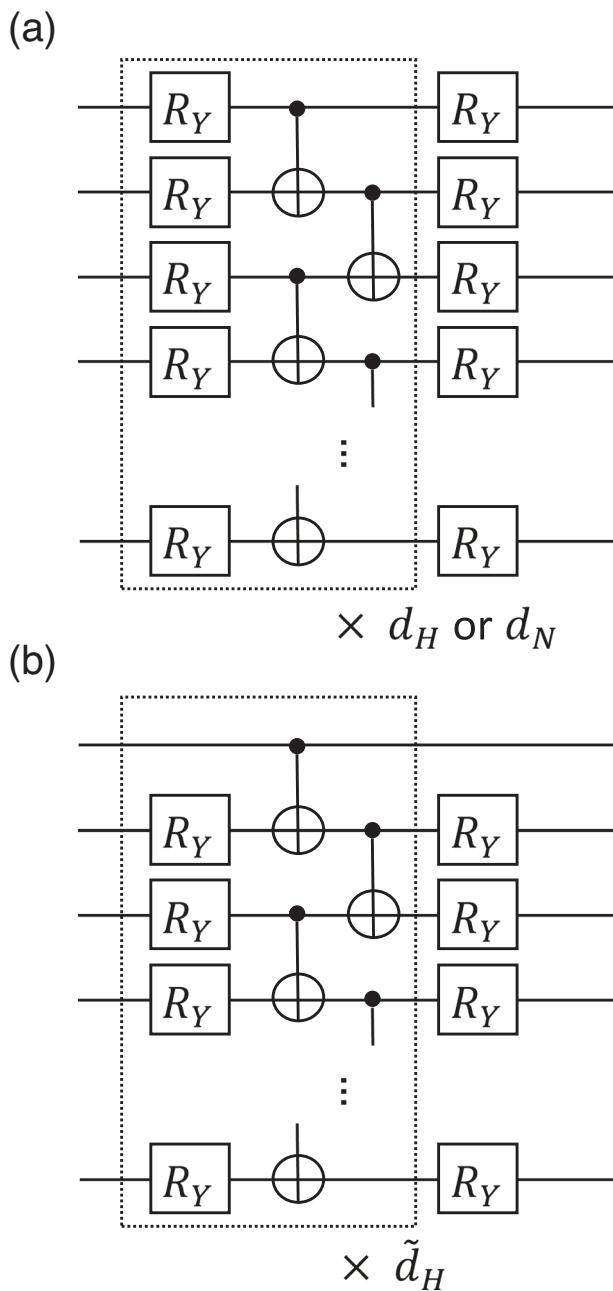


Fig. 4 | Circuits of real amplitude ansatz in this study. a Circuit in statevector procedure. All the lines represent system qubits. **b** Circuit in real device procedure. The topmost line represents an ancilla qubit and the other lines represent system qubits.

$nk(d_N + 1)$, respectively. We set $d_H = 4$ as a default by referring to the benchmark results in Supplementary Information 6. The initial parameters for HTN+VQE are chosen randomly from $[0, 1]$ and $[0, 2\pi]$ in the statevector and the real device procedure, respectively, and those for VQE are $[-2\pi, 2\pi]$. Note that only the results specifically relevant to the discussion are described in the main text, while the rest are presented in the supplementals.

In all the QMC methods (QMC, QC-QMC, and HTN+QMC), we evaluate the mean and standard deviation of the (projected) energy over 5,000 to 100,000 iterations excluding the Heisenberg chain model, whereas 50,000 to 100,000 iterations in the Heisenberg chain model. Hereafter absolute deviation from the exact ground state is referred to by energy difference. In QMC, a leading single orthonormal basis state in the exact ground state (single reference state hereafter) is chosen as a trial wave

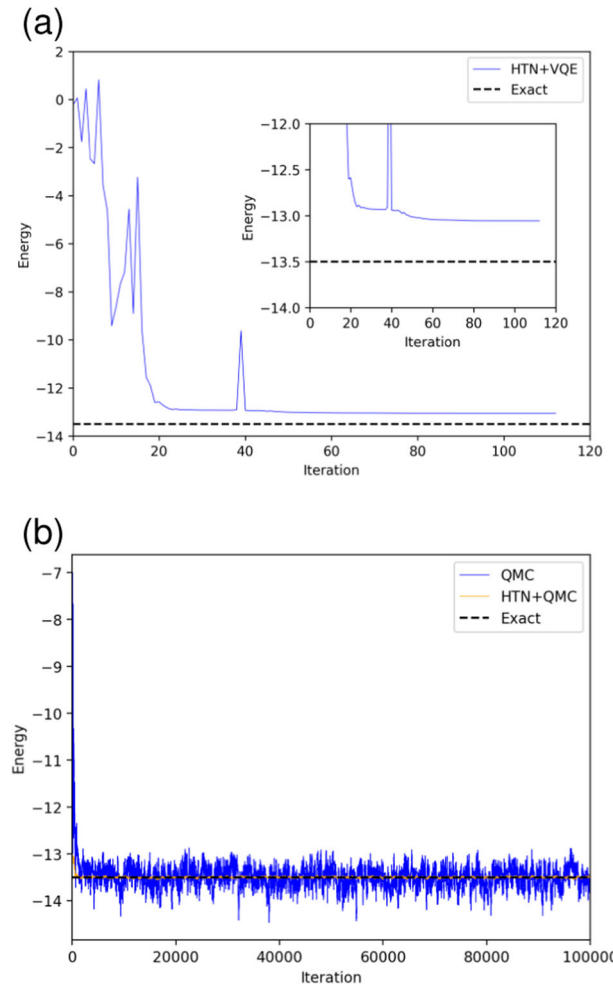


Fig. 5 | Results of the energy in the Heisenberg chain models of the cluster setting with $n = 4$, $k = 2$, $J_{\text{inter}} = 1.0$, and $d_H = 4$. The black dashed line represents the energy of the exact ground state. a Result for HTN+VQE (blue line). The inset shows the enlarged view along the y-axis. **b** Results for QMC (blue line) and HTN+QMC (orange line).

function. See Supplementary Information 7 for the details of the VQE and QMC conditions.

Statevector simulation

Figure 5a shows the result of executing HTN+VQE for the Heisenberg chain model in the cluster setting with $d_H = 4$, $k = 2$, and $J_{\text{inter}} = 1.0$. As in the inset, the energy difference from the exact ground state energy is 4.4×10^{-1} at the end of the optimization. Figure 5b shows the result for HTN+QMC, and the energy difference with standard deviation from the exact value is $1.1 \times 10^{-4} \pm 1.4 \times 10^{-2}$, which is more accurate than QMC. Specifically, that for QMC is $2.5 \times 10^{-2} \pm 2.1 \times 10^{-1}$. We discuss the details of this improvement in Sec. III, and we note the measurement cost scale in the QMC step of HTN+QMC in Sec. IV D.

Here, we briefly comment on the other models; the computational results are described in detail in Supplementary Information 6. Table 1 shows the results summarized on HTN of the Heisenberg chain models with $k = 2$ and 3, the graphite model, the hydrogen plane model with ID 3, and MABI. In all the models, the variance for HTN+QMC is smaller than that for HTN+VQE or QMC. Except for the hydrogen plane model, the variance decreases as the fidelity increases. Here, the fidelity is defined as the square of the overlap between the target and exact ground states. See Supplementary Information 2 for the statistical analysis for the fidelity and the variance in simple cases. For the hydrogen plane

Table 1 | Energy differences with a standard deviation in VQE, QMC, and HTN+QMC, and fidelity for HTN+VQE and the single reference state for the Heisenberg chain models of the cluster setting with $k = 2$ and 3 and $J_{\text{inter}} = 1.0$, the graphite model of the horizontal setting with $k = 2$, the hydrogen plane model of HOMO-LUMO setting with $k = 2$ and ID 3, and MABI of HOMO-LUMO setting with $k = 3$; $n = 4$ and $d_H = 4$ for all the models

| Models | HTN+VQE | QMC | HTN+QMC | Fidelity (HTN+VQE) | Fidelity (single reference state) |
|------------------------------|----------------------|---|---|--------------------|-----------------------------------|
| Heisenberg chain ($k = 2$) | 4.4×10^{-1} | $2.5 \times 10^{-2} \pm 2.1 \times 10^{-1}$ | $1.1 \times 10^{-4} \pm 1.4 \times 10^{-2}$ | 0.92 | 0.13 |
| Heisenberg chain ($k = 3$) | 1.0×10^0 | $3.0 \times 10^{-2} \pm 5.5 \times 10^{-1}$ | $3.0 \times 10^{-3} \pm 3.0 \times 10^{-2}$ | 0.80 | 0.06 |
| Graphite | 6.4×10^{-4} | $4.6 \times 10^{-4} \pm 6.4 \times 10^{-2}$ | $8.1 \times 10^{-6} \pm 8.6 \times 10^{-5}$ | 1.00 | 0.09 |
| Hydrogen plane | 3.5×10^{-2} | $9.1 \times 10^{-4} \pm 6.7 \times 10^{-3}$ | $3.0 \times 10^{-5} \pm 1.5 \times 10^{-3}$ | 0.44 | 0.45 |
| MABI | 2.4×10^{-2} | $6.6 \times 10^{-5} \pm 2.6 \times 10^{-3}$ | $9.2 \times 10^{-6} \pm 1.5 \times 10^{-3}$ | 0.94 | 0.86 |

The energy unit is Hartree.

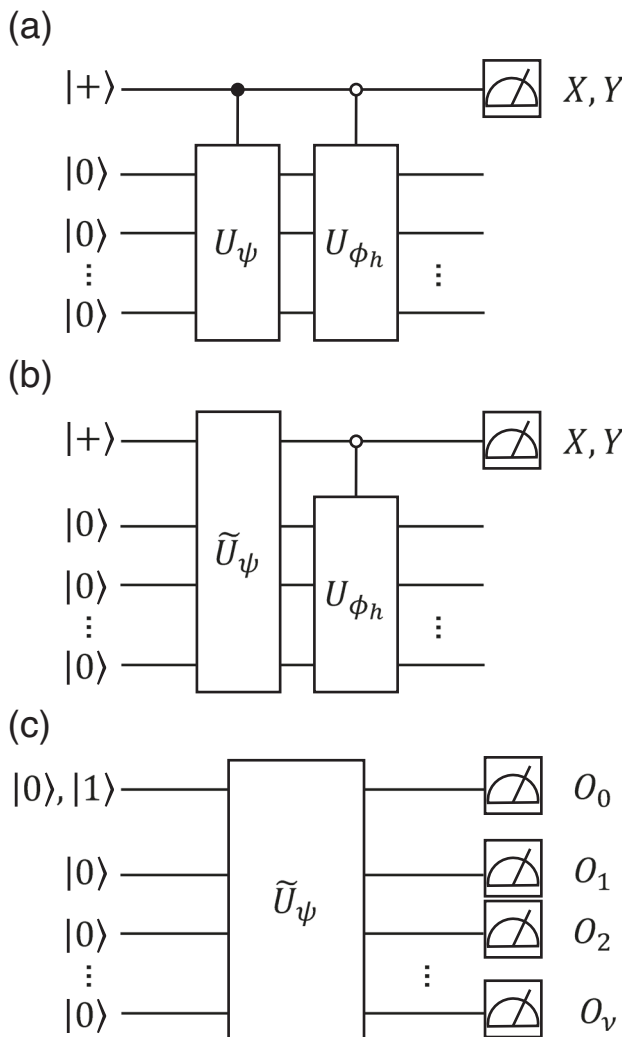


Fig. 6 | Quantum circuits for calculating the overlap. The topmost line represents the ancilla qubit, and the other lines the system qubits. **a** Hadamard test. **b** Pseudo-Hadamard test. **c** VQE circuit with constraint to determine \tilde{U}_ψ used for the pseudo-Hadamard test. The ancilla qubit is set to $|0\rangle$ when calculating the constraints.

model, the variance for HTN+QMC is smaller than that for QMC, even though the fidelity for HTN+VQE (0.44) is almost the same as that for the single reference state (0.45). The fidelity is not the only factor that determines the quality of the trial wave function⁵². In the hydrogen plane model, the trial state generated by the HTN+VQE shares multiple determinants with the exact ground state, and it can make energy

estimation robust to fluctuations in the QMC wave function. Thus, the performance of QMC may be improved even if the trial wave function does not have high fidelity, and it is important to evaluate the trial wave function quality through QMC computation.

Real device experiments

We consider performing the proposed HTN+QMC algorithm on a real device. For this purpose, we need to reduce the overlap computational cost between the trial wave function and the orthonormal basis state (as in Eq. (4)). Conventionally, the overlap $\langle \psi | \phi_h \rangle$ between a wave function $|\psi\rangle = U_\psi |0\rangle^{\otimes v}$ and the orthonormal basis state $|\phi_h\rangle = U_{\phi_h} |0\rangle^{\otimes v}$, can be calculated using the Hadamard test, as in Fig. 6a, where U_ψ typically consists of a collection of one- and two-qubit gates depending on the ansatz and v is the number of system qubits. The controlled- U_ψ contains a much larger number of multi-qubit gates compared to U_ψ because all one- and two-qubit gates in U_ψ are modified to the controlled gates. Several techniques to calculate the overlaps in fermionic systems have been proposed that can avoid deep circuits, for example, by using the particle preserving ansatz^{21,53}. However, the techniques are inadequate for HTN+QMC due to no electron number preservation in the subsystems, and we explain the details in Supplementary Information 8.1. Note that U_{ϕ_h} requires at most v two-qubit gates because it applies the CNOT gates from the ancilla to target qubits, the latter of which is set to $|1\rangle$ in $|\phi_h\rangle$.

We develop a gate-efficient technique to calculate the overlap executable on an arbitrary ansatz called the pseudo-Hadamard test. See Supplementary Information 8 for extending the technique to HTN. Figure 6b shows the circuit of the pseudo-Hadamard test, in which U_ψ is replaced with \tilde{U}_ψ involving the ancilla qubit. This circuit calculates the overlap $\langle \tilde{\psi} | \phi_h \rangle$ if \tilde{U}_ψ satisfies the following conditions:

$$\begin{aligned} \tilde{U}_\psi |1\rangle |0\rangle^{\otimes v} &= |1\rangle |\tilde{\psi}\rangle, \\ \tilde{U}_\psi |0\rangle |0\rangle^{\otimes v} &= |0\rangle |0\rangle^{\otimes v}. \end{aligned} \quad (9)$$

The gate \tilde{U}_ψ can be determined through the VQE under constraints that the ancilla qubit is measured to be one in the first condition and all the qubits are measured to be zero in the second condition in Eq. (9), which is formulated as

$$\begin{aligned} \min_{\tilde{U}_\psi} \quad & \langle 1 | \langle 0 |^{\otimes v} \tilde{U}_\psi^\dagger (I \otimes H) \tilde{U}_\psi | 1 \rangle | 0 \rangle^{\otimes v} \\ \text{s.t.} \quad & \langle 1 | \langle 0 |^{\otimes v} \tilde{U}_\psi^\dagger (n_0 \otimes I^{\otimes v}) \tilde{U}_\psi | 1 \rangle | 0 \rangle^{\otimes v} = 1, \\ & \langle 0 | \langle 0 |^{\otimes v} \tilde{U}_\psi^\dagger \left(\sum_{\kappa=0}^v I^{\otimes \kappa} \otimes n_\kappa \right) \tilde{U}_\psi | 0 \rangle | 0 \rangle^{\otimes v} = 0, \end{aligned} \quad (10)$$

where the index of the ancilla qubit is set to 0. n_κ is the number operator of κ -th qubit in Eq. (8). Figure 6c shows the quantum circuit used to run such

VQE, where O_i ($i = 0, 1, \dots, \nu$) is an observable of the i -th qubit. The constraints can be relaxed through the appropriate selection of ansatz, such as the real amplitude ansatz without rotation gates on the ancilla qubit, as shown in Fig. 4b. In this case, VQE can be simplified as

$$\begin{aligned} \min_{\tilde{U}_\psi} \quad & \langle 1 | \langle 0 |^{\otimes \nu} \tilde{U}_\psi^\dagger (I \otimes H) \tilde{U}_\psi | 1 \rangle | 0 \rangle^{\otimes \nu} \\ \text{s.t.} \quad & \langle 0 | \langle 0 |^{\otimes \nu} \tilde{U}_\psi^\dagger \left(\sum_{\kappa=1}^{\nu} I^{\otimes \kappa} \otimes n_\kappa \right. \right. \\ & \left. \left. \otimes I^{\otimes \nu - \kappa} \right) \tilde{U}_\psi | 0 \rangle | 0 \rangle^{\otimes \nu} = 0. \end{aligned} \quad (11)$$

We adopt this simplified formalism hereafter. Note that $\tilde{U}_\psi | 0 \rangle | 0 \rangle^{\otimes \nu}$ takes either $| 0 \rangle | 0 \rangle^{\otimes \nu}$ or $-| 0 \rangle | 0 \rangle^{\otimes \nu}$ in the constraint, but the signs cancel out in a numerator and denominator of the projected energy in QC-QMC and HTN+QMC (see Eq. (14)), allowing one to ignore the sign. In cases where the technique is applied outside of QMC, the sign could be determined based on the overlap between a trial wave function and a specific orthonormal basis state, e.g., the Hartree-Fock state²¹. We also mention the extensions of the technique; a transition amplitude of $\langle \tilde{\psi} | \tilde{O} | \phi_h \rangle (\tilde{O} = I \otimes_{i=1}^{\nu} O_i)$ can be calculated by measuring each system qubit in the basis corresponding to O_i for the pseudo-Hadamard test circuit; that of $\langle \tilde{\psi} | \tilde{O} | \tilde{\psi}' \rangle$ can be also calculated by using the additional constraint $\langle 1 | \langle 0 |^{\otimes \nu} \tilde{U}_\psi^\dagger \tilde{U}_\psi^\dagger \tilde{U}_\psi \left(\sum_{\kappa=1}^{\nu} I^{\otimes \kappa} \otimes n_\kappa \otimes I^{\otimes \nu - \kappa} \right) \tilde{U}_\psi^\dagger \tilde{U}_\psi | 1 \rangle | 0 \rangle^{\otimes \nu} = 0$, where $|\tilde{\psi}'\rangle$ is a trial wave function defined by \tilde{U}_ψ with a property of $\tilde{U}_\psi | 0 \rangle | 0 \rangle^{\otimes \nu} = | 0 \rangle | \tilde{\psi}' \rangle$, e.g., the ansatz changing the control qubit condition of CNOT gates in Fig. 4b from one to zero; a transition probability $|\langle \tilde{\psi} | \tilde{O} | \tilde{\psi}' \rangle|^2$ ^{54,55} can be trivially obtained by the square of the transition amplitude.

We applied the pseudo-Hadamard test technique to the HTN+QMC calculations on a real device *ibmq_kolkata* for the hydrogen plane model with ID 3 and MABI. The best trial wave function was selected from 100 seeds of HTN+VQE runs under the constraint ($\tilde{d}_H = 4$ and statevector execution), where at most five qubits including an ancilla qubit, are used in the overlap calculation. The energy accuracy decreased due to newly introduced constraints in the HTN+VQE, and thus we obtained the trial wave function of comparable accuracy by running 100 times, whereas the results without constraints in Table 1 were obtained with only one run. See Supplementary Information 8.2 for details on the extension to HTN and the calculation conditions. Figure 7a shows the result for the hydrogen plane model. A smaller fluctuation around the exact ground state energy was found in HTN+QMC than in QMC. The energy differences with a standard deviation obtained by the QMC, HTN+QMC (statevector) and HTN+QMC (*ibmq_kolkata*) are $9.1 \times 10^{-4} \pm 6.7 \times 10^{-3}$, $2.3 \times 10^{-5} \pm 1.5 \times 10^{-3}$, and $1.8 \times 10^{-5} \pm 1.8 \times 10^{-3}$ Hartree, respectively. Importantly, there is only a slight difference in the fluctuation between the real device and statevector, indicating that there would be some robustness of HTN+QMC to noises. A previous study¹⁸ showed that QC-QMC is robust to the depolarization noise. We also show the analytical and numerical result of the noise robustness in Supplementary Information 8.3, and the results show that such robustness also holds in the current settings of HTN+QMC, even though it might be significant in HTN+VQE. The MABI results in Fig. 7b also showed small variance in the real device experiment, where the results are $6.6 \times 10^{-5} \pm 2.6 \times 10^{-3}$, $2.3 \times 10^{-5} \pm 1.6 \times 10^{-3}$, and $4.2 \times 10^{-5} \pm 1.8 \times 10^{-3}$ Hartree in QMC, HTN+QMC (statevector) and HTN+QMC (*ibmq_kolkata*), respectively. These numerical and theoretical results suggest that HTN+QMC can be a promising candidate for calculating large systems beyond the scale of quantum devices while maintaining accuracy. Note that although we utilized the readout error mitigation and the dynamic decoupling in the overlap calculation, we confirmed that a comparable level of accuracy was achieved even without those options in HTN+QMC for the hydrogen plane model, where the energy difference with a standard deviation excluding the options is $2.6 \times 10^{-5} \pm 1.4 \times 10^{-3}$ Hartree.

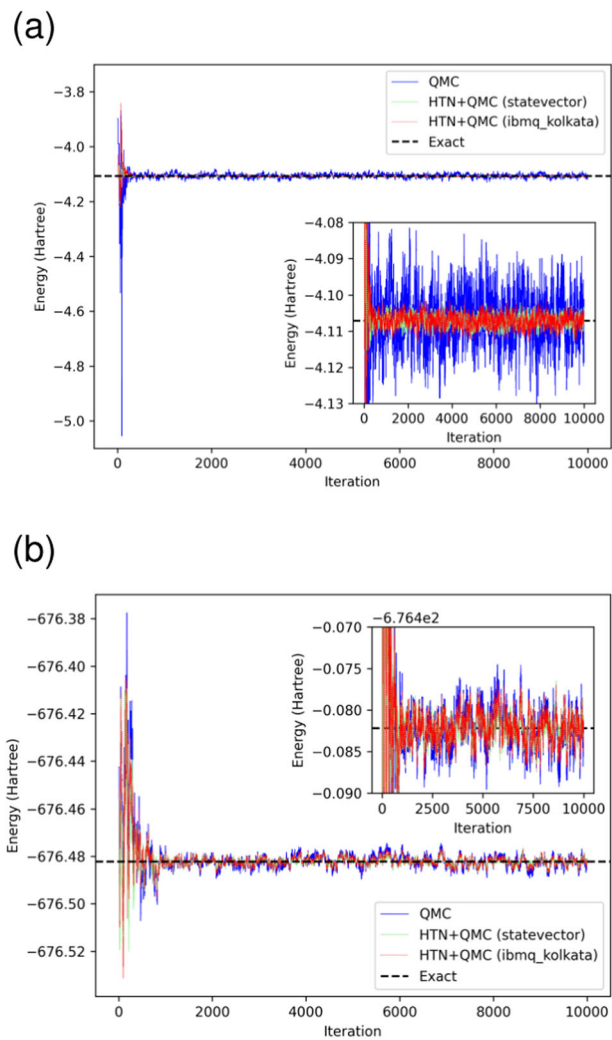


Fig. 7 | Results of the energy on the real device execution for the hydrogen plane model and MABI. HOMO-LUMO setting and $\tilde{d}_H = 4$ are adopted for the models. The blue line represents the QMC result, whereas the light green and red lines show the HTN+QMC results of the statevector and real device procedures, respectively. The exact ground state energy is depicted by the black dashed line. The inset in each figure presents an enlarged view along the y-axis. **a** Result of the hydrogen plane model with $n = 4$ and $k = 2$. **b** Result of MABI with $n = 4$ and $k = 3$.

Discussion

We discuss dependencies of accuracy on the system decompositions in HTN. We consider the Heisenberg chain model with $k = 2$, $n = 4$, and $J_{\text{inter}} = 1.0$, computed in the cluster, even-odd, and no-decomposition settings. Figure 8a-c show the decomposition dependencies of the fidelity, energy difference, and standard deviation for the Heisenberg chain model. In cases of the decomposition settings, the fidelity Fig. 8a in the cluster setting (0.92) is four times higher than that in the even-odd setting (0.22). We also calculated the bipartite entanglement entropy of the exact ground state when decomposing the cluster and even-odd settings to be 0.66 and 3.46, respectively. Thus, an appropriate choice of the decomposition setting is crucial in the performance of the trial wave function. The fidelity of the cluster setting is equal to or slightly higher than that for the no-decomposition setting with $d_N = 10$, whereas that for the even-odd setting is lower than that for the no-decomposition setting with $d_N = 2$. Here, the numbers of the parameters for the cluster setting with $d_H = 4$ and the no-decomposition setting with $d_N = 10$ are $nk(d_H + 1) + k(d_H + 1) = 50$ and $nk(d_N + 1) = 88$, respectively. That is, the cluster setting with fewer parameters shows comparable performance to the no-decomposition setting. The increase in fidelity is related to the decrease in the standard deviation of

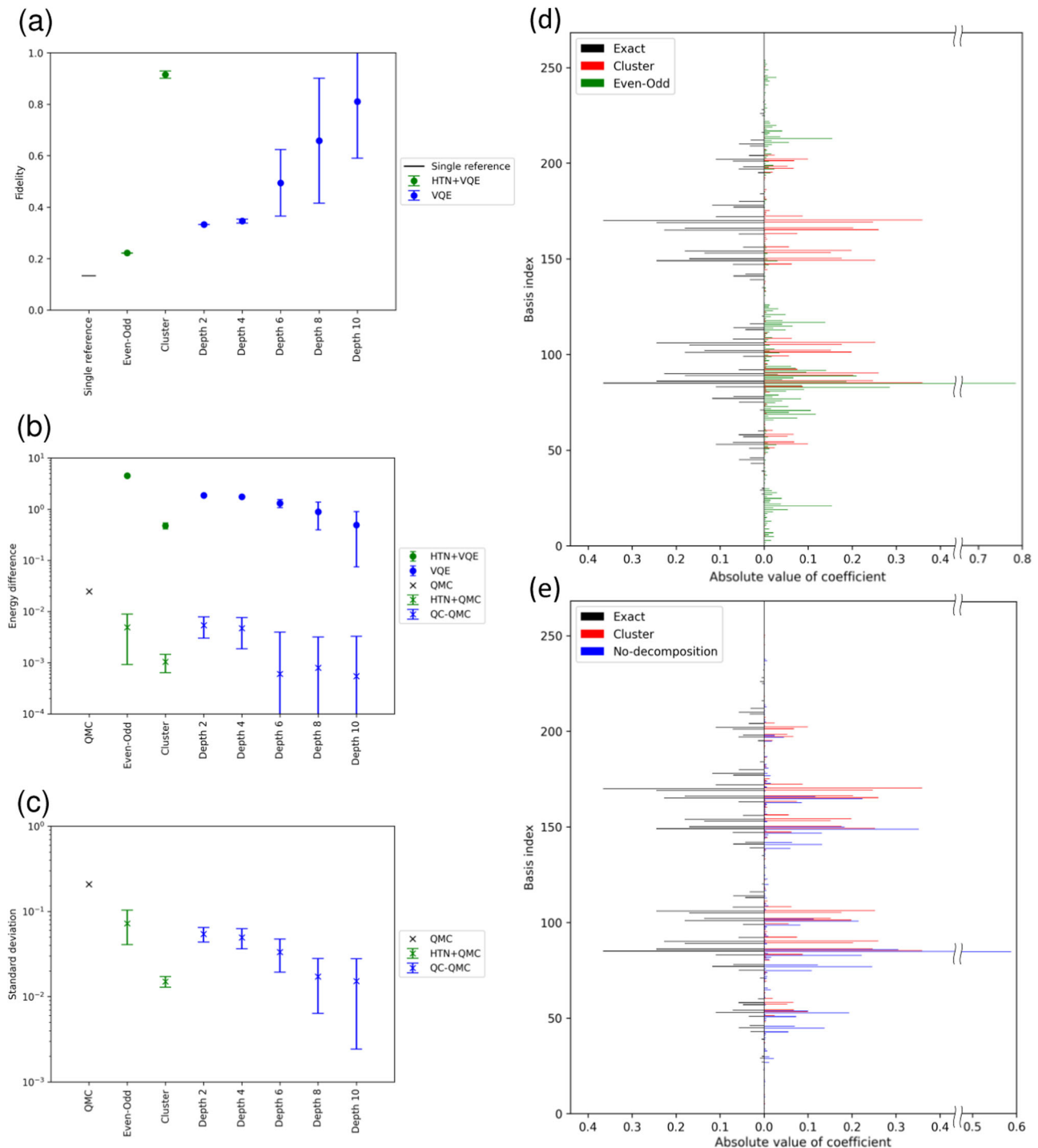


Fig. 8 | Results of the analysis for the Heisenberg chain model with $J_{\text{inter}} = 1.0$. **a-c** show the decomposition dependencies. The average and error bar is obtained over 10 different random seeds used for the initial parameters in VQE or HTN+VQE. The fidelity of the single reference state is plotted by the black bar in **(a)**, and the energy difference and standard deviation by the black cross markers in **(b, c)**, respectively. The green (blue) circle and cross markers denote the results for the decomposition (no-decomposition) setting in HTN+VQE and HTN+QMC (VQE and QC-QMC), respectively, with $d_H = 4$ ($d_N = 2, 4, \dots, 10$). In HTN+VQE and HTN+QMC, $n = 4$ and $k = 2$ for all the settings. **d, e** show the wave function distributions for the

Heisenberg chain model with $J_{\text{inter}} = 1.0$. The basis index is the value when the orthonormal basis state is expressed in the decimal number, e.g., $|10000010\rangle$ corresponds to 130. The black, red, green, and blue bars represent the coefficients for the exact ground state, HTN+VQE results with cluster setting, HTN+VQE results with even-odd setting, and VQE results with the no-decomposition setting, respectively. **a** Fidelity. **b** Energy difference. **c** Standard deviation. **d** Comparison of the exact ground state, cluster setting, and even-odd setting. **e** Comparison of the exact ground state, cluster setting, and no-decomposition setting ($d_N = 6$).

HTN+QMC as in Fig. 8c (and the decrease in the energy difference in HTN+VQE and HTN+QMC as in Fig. 8b. A similar tendency in fidelity, energy difference, and standard deviation can be found in the graphite model, the hydrogen plane model, and MABI (see Supplementary Information 9 for

details). These results suggest that if the system is appropriately decomposed, i.e., if the interaction between the subsystems is small, HTN can prepare a trial wave function that performs as well as or better than the wave function generated by the quantum circuit of the original system size. For quantitative

evaluations of the decomposition, we proposed measures in Supplementary Information 9, specifically, interaction strength between subsystems and mutual information. Note that one of the ways to increase the fidelity in VQE or HTN+VQE is to improve the initial wave function. As shown in Supplementary Information 9, the fidelity could increase in some cases by using the initial state which is close to the Hartree-Fock state. In addition, while the parameters of all the tensors are sequentially optimized in this study, separate optimization of one tensor by another could be an alternative⁵⁶.

The high performance in the cluster setting seems to arise when the wave function represented by QQT in Fig. 1a has a problem-inspired structure, whereas the ansatz used for each tensor is hardware efficient. To analyze the wave function in detail, we first compare the distribution of the absolute coefficient of the orthonormal basis state, calculated using one of the 10 random seeds in Fig. 8a–c. Figure. 8d shows the wave function distribution, where note that the value on the horizontal axis is the absolute value of the coefficient (not the square of the absolute value as in fidelity). The basis index is the value when the orthonormal basis state is expressed in the decimal number, e.g., $|10000010\rangle$ corresponds to 130. The cluster setting exhibits a distribution very close to that of the exact ground state compared to the even-odd setting. Note that for the even-odd setting, the distribution was calculated with the basis state encoding, where the qubit index was reordered from 8, 7, 6, 5/4, 3, 2, 1 to 8, 6, 4, 2/7, 5, 3, 1 as shown in Even-Odd of Fig. 3a. This qubit index was then changed back to that of Cluster in the plotting, allowing for direct comparison with the even-odd setting.

We next examine the wave function, represented as a linear combination of tensor products of the subsystems. In the cluster setting for the Heisenberg chain model, we approximately describe the exact ground state $|\psi_{g-C}\rangle$ using the four dominant terms with respective coefficients of $c_1 = -0.37$, $c_2 = 0.24$, $c_3 = -0.23$, and $c_4 = 0.18$, as

$$\begin{aligned} |\psi_{g-C}\rangle \simeq & c_1(|\mathbf{0101}\rangle \otimes |\mathbf{0101}\rangle + |\mathbf{1010}\rangle \otimes |\mathbf{1010}\rangle) \\ & + c_2(|\mathbf{0101}\rangle \otimes |\mathbf{0110}\rangle + |\mathbf{1001}\rangle \otimes |\mathbf{0101}\rangle) \\ & + |\mathbf{1010}\rangle \otimes |\mathbf{1001}\rangle + |\mathbf{0110}\rangle \otimes |\mathbf{1010}\rangle) \\ & + c_3(|\mathbf{1010}\rangle \otimes |\mathbf{0101}\rangle + |\mathbf{0101}\rangle \otimes |\mathbf{1010}\rangle) \\ & + c_4(|\mathbf{0101}\rangle \otimes |\mathbf{1001}\rangle + |\mathbf{0110}\rangle \otimes |\mathbf{0101}\rangle \\ & + |\mathbf{1001}\rangle \otimes |\mathbf{1010}\rangle + |\mathbf{1010}\rangle \otimes |\mathbf{0110}\rangle). \end{aligned} \quad (12)$$

The state is energetically favored because of the (sub)antiferromagnetic spin configurations, with at most one spin pair having the same parity (e.g., 00 and 11), considering that all terms in the Hamiltonian of Eqs. (5), (6), and (7) are positive. Each term consists of a *primitive* basis state (in bold) and the spin and spatial inverted states, where the ground state redefined in this primitive basis $\{|\mathbf{0101}\rangle, |\mathbf{1010}\rangle\} \otimes \{|\mathbf{0101}\rangle, |\mathbf{0110}\rangle\}$ is regarded as a *separable* state (with the same number of up/down spins in each subsystem), accurately prepared by the lower tensors with one leg connecting to the upper tensor. In case of the even-odd setting, where the qubit index is reordered and the number of up (or down) spins in the subsystem takes 0 to 4, the state in such a primitive basis, e.g., $\{|\mathbf{0000}\rangle \otimes |\mathbf{1111}\rangle, |\mathbf{0001}\rangle \otimes |\mathbf{1110}\rangle, |\mathbf{1100}\rangle \otimes |\mathbf{0011}\rangle, |\mathbf{1101}\rangle \otimes |\mathbf{0010}\rangle\}$, is no longer separable, resulting in a lower fidelity than in the cluster setting. Through the above mechanism, the decomposition setting affects the fidelity, where matching between the tensor network and target states is a crucial factor, being in analogy with the discussion in the area law with tensor networks. Note that the number of legs limits the dimension of the basis for state preparation.

HTN+VQE results with the cluster setting in Fig. 8d show that the coefficients for the above 12 basis states are of the same magnitude as c_1, c_2, \dots, c_4 . In contrast, the even-odd setting gives a much less accurate wave function; half of the basis states in Eq. (12) was negligibly small in magnitude, and the large coefficient of $|\mathbf{0101}\rangle \otimes |\mathbf{0101}\rangle$ is 0.78, leading to a different distribution from the exact.

Next, Fig. 8e shows the distribution of the no-decomposition setting, where the distributions of the ground state and cluster settings are reproduced

from Fig. 8a for comparison. The depth is set to $d_N = 6$ such that the number of parameters in the no-decomposition and cluster settings becomes comparable, that is, 50 and 48, respectively. The distribution for the no-decomposition setting deviates from that for the exact wave function, and half of the basis states in Eq. (12) were negligibly small in magnitude. The no-decomposition setting would achieve higher performance than HTN. However, when the number of ansatz parameters is restricted, HTN may perform better if we find an ansatz and decomposition suited to the structure of the system. In fact, the coefficient of the basis state $|\mathbf{00101101}\rangle$, which has the 10-th largest magnitude in the no-decomposition setting, is 0.14; in contrast, the corresponding values are -0.057 in the ground state and -0.00018 in the cluster setting. Thus, the cluster setting can efficiently prepare a trial wave function that incorporates system correlations with fewer parameters by eliminating the basis states with a small contribution to the ground state of the system. Note that these observations are verified by calculating over 10 random seeds.

As summary, we proposed an algorithm HTN+QMC that combines QC-QMC with HTN for calculating quantum chemistry problems beyond the size of a quantum device. As demonstrated on the benchmark models, our algorithm exhibits energy with smaller variance than QMC. We developed the gate-efficient pseudo-Hadamard test technique involving an ancilla qubit for conducting HTN+QMC experiments on real devices; the at most five qubits experiment showed an accuracy comparable to the state-vector simulation for the hydrogen plane models (8 qubit model) and MAB (12 qubit model).

While this study assumed the target system size to be larger than that of the quantum device, there may be cases in which the proposed algorithm should be used even if the target system size equals that of the quantum device. For example, a quantum computer with thousands of qubits has appeared⁵⁷. However, an accurate solution may not be obtained when calculating a chemical model of that size owing to noise in the quantum device. In such a case, decomposing the system into subsystems of about hundreds of qubits would lead to a more accurate result than that obtained by directly executing on a thousand qubits. In addition, the tree tensor that we have assumed has the advantage that the computation of the lower tensor can be performed in parallel.

The research on QC-QMC has not yet been extensive, and applying techniques developed for NISQ devices to QC-QMC is a possible future research item, as in HTN in this study. HTN is also an intriguing research area, where there are several classical decomposition approaches, which may inspire ideas for efficient quantum algorithms to deal with the correlations between subsystems^{58–61}. Another interesting direction is applying QC-QMC to fields outside the electronic structure calculations such as machine learning for designing advanced materials.

Methods

Variational quantum eigensolver

Variational quantum eigensolver (VQE) takes a variational approach to obtain the ground state of a given Hamiltonian. Here, a trial wave function $|\psi(\vec{\theta})\rangle$ is generated by a quantum circuit with variational parameters $\vec{\theta}$, which is repeatedly updated using the classical computer until a termination condition is satisfied, e.g., the expectation value of the Hamiltonian $\langle\psi(\vec{\theta})|H|\psi(\vec{\theta})\rangle$ takes a minimum. The expressibility of $|\psi(\vec{\theta})\rangle$ depends on the quantum circuit, called ansatz. There are several problem-inspired ansatze, such as the unitary coupled cluster ansatz⁶² and Hamiltonian variational ansatz⁶³. However, despite the high performance, the ansatz requires deeper quantum gates. In real device experiments, compromised strategy with hardware-efficient ansatze⁶⁴ is often considered.

The Hamiltonian H in the electronic structure problems can be represented as

$$H = \sum_a c_a \bigotimes_b P_{ab}, \quad (13)$$

where c_a is the a -th coefficient of H and $P_{ab} \in \{X, Y, Z, I\}$ is the a -th Pauli or identity operator on the b -th site. In this study, we assume $c_a \in \mathbb{R}$ in all models (although $c_a \in \mathbb{C}$ in general). The number of terms is estimated to be $\mathcal{O}(N_{so}^4)$ with N_{so} being the number of spin-orbitals⁶⁵. We choose the Jordan-Wigner mapping⁶⁶ for the fermion-qubit translation.

Quantum computing quantum Monte Carlo

In QC-QMC¹⁸, a stochastic algorithm such as the imaginary-time evolution is used to iteratively update the discretized coefficients of the wave function, i.e., walkers. As we explained in Sec. I, This study will validate a version of QC-QMC that uses quantum computation only for energy evaluation²¹. The following projected energy E_{proj} is used as a common energy estimator:

$$E_{\text{proj}} = \frac{\langle \xi | H | \psi_{\text{QMC}} \rangle}{\langle \xi | \psi_{\text{QMC}} \rangle}, \quad (14)$$

where $|\xi\rangle$ is a trial wave function. $|\psi_{\text{QMC}}\rangle$ denotes a wave function generated by QMC, defined as

$$|\psi_{\text{QMC}}\rangle = \sum_h w_h |\phi_h\rangle, \quad (15)$$

where w_h is the h -th coefficient and is expressed using discretized units (walkers). $|\phi_h\rangle$ is the h -th orthonormal basis state as in a Slater determinant and can be represented by a binary string, i.e., a computational basis. The procedure of generating the wave function $|\psi_{\text{QMC}}\rangle$ depends on the QMC method. In this work, we choose FCIQMC. See Supplementary Information 1 for process details. E_{proj} is not equivalent to the expectation value of the Hamiltonian $\langle \psi_{\text{QMC}} | H | \psi_{\text{QMC}} \rangle / \langle \psi_{\text{QMC}} | \psi_{\text{QMC}} \rangle$ (that is, not the pure estimator); however, we can obtain the exact ground state energy E_g when $|\psi_{\text{QMC}}\rangle$ approaches the ground state $|\psi_g\rangle$, i.e., $|\psi_{\text{QMC}}\rangle \sim |\psi_g\rangle$ as

$$E_{\text{proj}} \sim \frac{\langle \xi | H | \psi_g \rangle}{\langle \xi | \psi_g \rangle} = E_g, \quad (16)$$

where $H|\psi_g\rangle = E_g|\psi_g\rangle$ is used.

The trial function $|\xi\rangle$ is fixed throughout the QMC, and a more sophisticated $|\xi\rangle$ can be used to lower the statistical error. A trivial case is that, if the trial wave function coincides with the ground state, i.e., $|\xi\rangle = |\psi_g\rangle$, then we can obtain E_g for any $|\psi_{\text{QMC}}\rangle$ with zero variance⁶⁷. See Supplementary Information 2 for derivation details. For example, the Hartree-Fock state, the linear combination of mean-field states, and the Jastrow-type states²⁵ are used as the trial wave functions conveniently available in classical computations. Therefore, we can considerably minimize energy estimation errors by preparing a suboptimal trial wave function in the exponentially large Hilbert space.

In QC-QMC, trial wave function $|\xi\rangle$ is prepared by a quantum algorithm. Specifically, by decomposing $|\psi_{\text{QMC}}\rangle$, Eq. (14) is rewritten as

$$E_{\text{proj}} = \frac{\sum_h w_h \langle \xi | \phi_h \rangle \langle \phi_h | H | \phi_h \rangle}{\sum_h w_h \langle \xi | \phi_h \rangle}. \quad (17)$$

The matrix elements $\langle \phi_h | H | \phi_h \rangle$ can be obtained by trivial classical calculations. In contrast, quantum computation is required to calculate the overlap ($\langle \xi | \phi_h \rangle$ and $\langle \xi | \phi_h \rangle$) for which the Hadamard test or classical shadow can be applied^{68,69}, henceforth, $\langle \xi | \phi_h \rangle$ and $\langle \xi | \phi_h \rangle$ will both be described as $\langle \xi | \phi_h \rangle$. We discuss in Supplementary Information 2 that the variance of projected energy will decrease with the fidelity of the trial wave function in a simplified case. In this study, fidelity is defined as the square of the overlap between the target and ground states, assuming zero noise.

Hybrid tensor network

In the two-layer QQTN, the original nk -qubit system is decomposed into k subsystems of n qubit states $|\varphi^{i_m}\rangle$, which are integrated with the k -qubit state $|\psi\rangle$. These states can be associated with tensors, defined as the lower tensor $\varphi_{\vec{j}_m}^{i_m} = \langle \vec{j}_m | \varphi^{i_m} \rangle$ and upper tensor $\psi_{\vec{i}} = \langle \vec{i} | \psi \rangle$ with the vector indices $\vec{j}_m = j_{m1} j_{m2} \dots j_{mn}$ and $\vec{i} = i_1 i_2 \dots i_k$ in n -qubit and k -qubit binary strings, respectively. The wave function $|\psi_{\text{HTN}}\rangle$ is then decomposed into tensor products of $|\varphi^{i_m}\rangle$

$$|\psi_{\text{HTN}}\rangle = \sum_{\vec{i}} \psi_{\vec{i}} \bigotimes_{m=1}^k |\varphi^{i_m}\rangle, \quad (18)$$

which is the same as Eq. (1) although omitting the parameters, where the number of vector coefficients $\{\psi_{\vec{i}}\}$ is 2^{Lk} with L denoting the number of bits (legs) used to construct each i_m . $L = 1$ is adopted in this study. If $L = n$, $|\psi_{\text{HTN}}\rangle$ becomes the general nk -qubits wave function. When $L \ll n$, $|\psi_{\text{HTN}}\rangle$ lives in a subspace much smaller than the entire 2^{nk} dimensional Hilbert space; however, it can be larger than the subspace consisting only of the classical tensor due to the exponentially large ranks of $\psi_{\vec{i}}$ and $\varphi_{\vec{j}_m}^{i_m}$. Moreover, the performance of QQTN depends on the decomposition setting of the system, which determines the entanglement between the subsystems.

Tensor-network quantum circuits can be implemented in various ways. For example, we can define a lower tensor as $|\varphi^{i_m}\rangle = U_{Lm} |i_m\rangle |0\rangle^{\otimes n-1}$, $U_{Lm} |i_m\rangle^{\otimes n}$, $U_{Lm}^{\dagger} |0\rangle^{\otimes n}$, etc., where the first two formulations give the index in initial states and the third a unitary matrix using unitary matrices U_{Lm} and U_{Lm}^{\dagger} . In the present study, we choose $|\varphi^{i_m}\rangle = U_{Lm} |i_m\rangle |0\rangle^{\otimes n-1}$ and $|\psi\rangle = U_U |0\rangle^{\otimes k}$ for lower and upper tensors, respectively.

In our QQTN formulation, an observable is defined as the tensor product $O = \bigotimes_{m,r} O_{mr}$, where O_{mr} is observable on the r -th qubit of the m -th subsystem (lower tensor). Transition amplitude is then defined as

$$T = \langle \psi_{\text{HTN}}^{(1)} | O | \psi_{\text{HTN}}^{(2)} \rangle, \quad (19)$$

which is the same as Eq. (2) although omitting the parameters, where $|\psi_{\text{HTN}}^{(l)}\rangle = \sum_{\vec{i}} \psi_{\vec{i}}^{(l)} \bigotimes_{m=1}^k |\varphi^{i_m(l)}\rangle$ ($l = 1, 2$) are the two different of states for $|\psi_{\text{HTN}}\rangle$. As explained in the next section, T is used in VQE and QMC to evaluate an observable and overlap, respectively.

We first calculate $N_{m1}^{i_m(1)i_m(2)} = \langle \varphi^{i_m(1)} | \bigotimes_r O_{mr} | \varphi^{i_m(2)} \rangle$ for the lower tensors by quantum computations, construct $N_m = \begin{pmatrix} N^{00} & N^{01} \\ N^{10} & N^{11} \end{pmatrix}$, which is a trivial classical process, and then integrate the results as $T = \langle \psi^{(1)} | \bigotimes_m N_m | \psi^{(2)} \rangle$ on the upper tensor by quantum computations. Supplementary Information 3 shows the details of this procedure, which is based on the Hadamard test circuit as in Ref. 70. Our algorithm requires only $\max(n, k)$ qubits except for ancilla qubits. In this study, only $8k + 2$ terms are measured to calculate T ; i.e., the overhead for calculating the expectation value is a linear scale for the system size nk . Note that the number of measurements is $2 \times 4^L k + 2$ in general.

Proposed algorithm: HTN+QMC

The procedure of HTN+QMC consists of two steps.

1. Perform VQE by minimizing $\langle \psi_{\text{HTN}} | H | \psi_{\text{HTN}} \rangle$ to obtain trial wave function $|\xi\rangle = |\psi_{\text{HTN}}\rangle$.

2. Perform QC-QMC by using the obtained trial wave function $|\psi_{\text{HTN}}\rangle$; the quantum computer is used to compute E_{proj} to accurately estimate the ground state energy.

Here, we will denote HTN+VQE when only the first step is mentioned. HTN+QMC can be performed for nk -qubit system by using only $\mathcal{O}(\max(n, k))$ qubits except for ancilla qubits. The Hamiltonian and projected energy can be evaluated in both steps by calculating T in Eq. (19).

In the first step, by splitting index b in Eq. (13) into indices m and r , we can rewrite H and its expectation value as

$$H = \sum_a c_a \bigotimes_{m,r} P_{amr}, \quad (20)$$

and

$$\langle \psi_{\text{HTN}} | H | \psi_{\text{HTN}} \rangle = \sum_a c_a \langle \psi_{\text{HTN}} | \bigotimes_{m,r} P_{amr} | \psi_{\text{HTN}} \rangle, \quad (21)$$

respectively. The expectation value is evaluated through Eq. (19) by setting $|\psi_{\text{HTN}}^{(1)}\rangle = |\psi_{\text{HTN}}^{(2)}\rangle = |\psi_{\text{HTN}}\rangle$ and replacing O_{mr} with P_{amr} ; coefficient index a is implicitly included in the expression for O_{mr} . The wave function $|\psi_{\text{HTN}}\rangle$ is prepared by parameterized quantum circuits equivalent to the unitary matrices U_{Lm} and U_U .

In the second step, the overlap $\langle \xi | \phi_h \rangle = \langle \psi_{\text{HTN}} | \phi_h \rangle$ in Eq. (17) is calculated by substituting $|\psi_{\text{HTN}}^{(1)}\rangle = |\psi_{\text{HTN}}\rangle$, $|\psi_{\text{HTN}}^{(2)}\rangle = |\phi_h\rangle$, and $O = I^{\otimes nk}$ in T in Eq. (19), where the circuit parameters are fixed to the values obtained in the first step. Specifically, we can prepare an arbitrary basis state $|\phi_h\rangle = \bigotimes_{m,r} |j_{mr}(h)\rangle = (\bigotimes_{m,r} X^{j_{mr}(h)}) |0\rangle^{\otimes nk}$ by setting $U_U^{(2)} = I^{\otimes k}$ and $U_{Lm}^{(2)} = \bigotimes_m X^{j_{mr}(h)}$, where $j_{mr}(h)$ is a function of h and takes a value on $\{0, 1\}$, and X is the Pauli X operator. Using the overlaps $\langle \psi_{\text{HTN}} | \phi_h \rangle$ of all $|\phi_h\rangle$, corresponding to the orthonormal basis states appearing through the QMC wave function and matrix elements $\langle \phi_h | H | \phi_h \rangle$ during the QMC execution at hand, we can perform QMC through iterative evaluations of the projected energy (Eqs. (14) and (17)) in principle. The scale of the measurement cost in the QMC step is $\mathcal{O}(N_{\text{so}}^4 N_W^* (\tau_{\text{fin}}/\Delta\tau)^{2L} k/\varepsilon^2)$, where N_{so} comes from $\langle \phi_h | H | \phi_h \rangle$, N_W^* is the maximum number of walkers that can be taken in a QMC iteration, τ_{fin} is a total time in QMC, $\Delta\tau$ is a time step in QMC, $2^{2L}k$ comes from the overhead of HTN contraction, ε is an additive error^{43,71}. We mention that in our actual run, for simplicity, the overlaps of all orthonormal basis states were computed before QMC in the statevector simulation. For real device execution, the overlaps of the states for all target electron numbers were computed.

Data availability

The details of calculation conditions are presented in this paper and Supplementary Information. Additional data in this work are available from the corresponding author upon reasonable request.

Code availability

The codes in this work are available from the corresponding author upon reasonable request.

Received: 13 November 2023; Accepted: 17 May 2024;

Published online: 06 June 2024

References

1. Ceder, G. et al. Identification of cathode materials for lithium batteries guided by first-principles calculations. *Nature* **392**, 694–696 (1998).
2. Gao, Q. et al. Computational investigations of the lithium superoxide dimer rearrangement on noisy quantum devices. *J. Phys. Chem. A* **125**, 1827–1836 (2021).
3. Nørskov, J. K., Bligaard, T., Rossmeisl, J. & Christensen, C. H. Towards the computational design of solid catalysts. *Nat. Chem.* **1**, 37–46 (2009).
4. Turro, N. J. *Modern Molecular Photochemistry* (University Science Books, 1991).
5. Michl, J. & Bonacic-Koutecky, V. *Electronic Aspects of Organic Photochemistry* (Wiley, 1990).
6. Bauer, B., Bravyi, S., Motta, M. & Kin-Lic Chan, G. Quantum algorithms for quantum chemistry and quantum materials science. *Chem. Rev.* **120**, 12685–12717 (2020).
7. Preskill, J. Quantum computing in the NISQ era and beyond. *Quantum* **2**, 79 (2018).
8. Bharti, K. et al. Noisy intermediate-scale quantum algorithms. *Rev. Mod. Phys.* **94**, 015004 (2022).
9. Cerezo, M. et al. Variational quantum algorithms. *Nat. Rev. Phys.* **3**, 625–644 (2021).
10. Peruzzo, A. et al. A variational eigenvalue solver on a photonic quantum processor. *Nat. Commun.* **5**, 4213 (2014).
11. Yu, Kitaev, A. Quantum measurements and the abelian stabilizer problem. Preprint at <https://arxiv.org/abs/quant-ph/9511026> (1995).
12. Stilck França, D. & García-Patrón, R. Limitations of optimization algorithms on noisy quantum devices. *Nat. Phys.* **17**, 1221–1227 (2021).
13. McClean, J. R., Boixo, S., Smelyanskiy, V. N., Babbush, R. & Neven, H. Barren plateaus in quantum neural network training landscapes. *Nat. Commun.* **9**, 4812 (2018).
14. Grant, E., Wossnig, L., Ostaszewski, M. & Benedetti, M. An initialization strategy for addressing barren plateaus in parametrized quantum circuits. *Quantum* **3**, 214 (2019).
15. Skolik, A., McClean, J. R., Mohseni, M., van der Smagt, P. & Leib, M. Layerwise learning for quantum neural networks. *Quantum Mach. Intell.* **3**, 5 (2021).
16. Cerezo, M., Sone, A., Volkoff, T., Cincio, L. & Coles, P. J. Cost function dependent barren plateaus in shallow parametrized quantum circuits. *Nat. Commun.* **12**, 1791 (2021).
17. Kanno, K. et al. Quantum-Selected configuration interaction: classical diagonalization of hamiltonians in subspaces selected by quantum computers. Preprint at <https://arxiv.org/abs/2302.11320> (2023).
18. Huggins, W. J. et al. Unbiasing fermionic quantum monte carlo with a quantum computer. *Nature* **603**, 416–420 (2022).
19. Yang, Y., Lu, B.-N. & Li, Y. Accelerated quantum monte carlo with mitigated error on noisy quantum computer. *PRX Quantum* **2**, 040361 (2021).
20. Tan, K. C., Bhowmick, D. & Sengupta, P. Sign-problem free quantum stochastic series expansion algorithm on a quantum computer. *npj Quantum Inf.* **8**, 1–7 (2022).
21. Xu, X. & Li, Y. Quantum-assisted monte carlo algorithms for fermions. *Quantum* **7**, 1072 (2023).
22. Zhang, Y., Huang, Y., Sun, J., Lv, D. & Yuan, X. Quantum computing quantum monte carlo. Preprint at <http://arxiv.org/abs/2206.10431> (2022).
23. Layden, D. et al. Quantum-enhanced markov chain monte carlo. *Nature* **619**, 282–287 (2023).
24. Lee, J. et al. Response to “exponential challenges in unbiasing quantum monte carlo algorithms with quantum computers”. Preprint at <http://arxiv.org/abs/2207.13776> (2022).
25. Austin, B. M., Zubarev, D. Y. & Lester Jr, W. A. Quantum monte carlo and related approaches. *Chem. Rev.* **112**, 263–288 (2012).
26. Al-Hamdani, Y. S. et al. Interactions between large molecules pose a puzzle for reference quantum mechanical methods. *Nat. Commun.* **12**, 3927 (2021).
27. McMillan, W. L. Ground state of liquid He⁴. *Phys. Rev.* **138**, A442–A451 (1965).
28. Ceperley, D., Chester, G. V. & Kalos, M. H. Monte carlo simulation of a many-fermion study. *Phys. Rev.* **16**, 3081–3099 (1977).

29. Blankenbecler, R., Scalapino, D. J. & Sugar, R. L. Monte carlo calculations of coupled boson-fermion systems. I. *Phys. Rev. D* **24**, 2278–2286 (1981).

30. Sugiyama, G. & Koonin, S. E. Auxiliary field Monte-Carlo for quantum many-body ground states. *Ann. Phys.* **168**, 1–26 (1986).

31. Booth, G. H., Thom, A. J. W. & Alavi, A. Fermion monte carlo without fixed nodes: a game of life, death, and annihilation in slater determinant space. *J. Chem. Phys.* **131**, 054106 (2009).

32. Takeshita, T. et al. Increasing the representation accuracy of quantum simulations of chemistry without extra quantum resources. *Phys. Rev. X* **10**, 011004 (2020).

33. Roos, B. O. The complete active space self-consistent field method and its applications in electronic structure calculations. In *Advances in Chemical Physics, Advances in chemical physics*, 399–445 (John Wiley & Sons, Inc., Hoboken, NJ, USA, 2007).

34. Yamazaki, T., Matsuura, S., Narimani, A., Saidmuradov, A. & Zaribafyan, A. Towards the practical application of Near-Term quantum computers in quantum chemistry simulations: A problem decomposition approach. Preprint at <http://arxiv.org/abs/1806.01305> (2018).

35. Fujii, K. et al. Deep variational quantum eigensolver: A Divide-And-Conquer method for solving a larger problem with smaller size quantum computers. *PRX Quantum* **3**, 010346 (2022).

36. Kawashima, Y. et al. Optimizing electronic structure simulations on a trapped-ion quantum computer using problem decomposition. *Commun. Phys.* **4**, 1–9 (2021).

37. Greene-Diniz, G. et al. Modelling carbon capture on metal-organic frameworks with quantum computing. *EPJ Quantum Technol.* **9**, 37 (2022).

38. Cao, C. et al. Ab initio quantum simulation of strongly correlated materials with quantum embedding. Preprint at <http://arxiv.org/abs/2209.03202> (2022).

39. Peng, T., Harrow, A. W., Ozols, M. & Wu, X. Simulating large quantum circuits on a small quantum computer. *Phys. Rev. Lett.* **125**, 150504 (2020).

40. Harada, H., Wada, K. & Yamamoto, N. Optimal parallel wire cutting without ancilla qubits. Preprint at <http://arxiv.org/abs/2303.07340> (2023).

41. Sun, J. et al. Perturbative quantum simulation. *Phys. Rev. Lett.* **129**, 120505 (2022).

42. Huggins, W., Patil, P., Mitchell, B., Birgitta Whaley, K. & Miles Stoudenmire, E. Towards quantum machine learning with tensor networks. *Quantum Sci. Technol.* **4**, 024001 (2019).

43. Yuan, X., Sun, J., Liu, J., Zhao, Q. & Zhou, Y. Quantum simulation with hybrid tensor networks. *Phys. Rev. Lett.* **127**, 040501 (2021).

44. Schollwöck, U. The density-matrix renormalization group in the age of matrix product states. *Ann. Phys.* **326**, 96–192 (2011).

45. Verstraete, F. & Cirac, J. I. Renormalization algorithms for Quantum-Many body systems in two and higher dimensions. Preprint at <https://arxiv.org/abs/cond-mat/0407066> (2004).

46. Shi, Y.-Y., Duan, L.-M. & Vidal, G. Classical simulation of quantum many-body systems with a tree tensor network. *Phys. Rev. A* **74**, 022320 (2006).

47. Eddins, A. et al. Doubling the size of quantum simulators by entanglement forging. *PRX Quantum* **3**, 010309 (2022).

48. Motta, M. et al. Quantum chemistry simulation of ground- and excited-state properties of the sulfonium cation on a superconducting quantum processor. *Chem. Sci.* **14**, 2915–2927 (2023).

49. Motta, M. et al. Determining eigenstates and thermal states on a quantum computer using quantum imaginary time evolution. *Nat. Phys.* **16**, 205–210 (2019).

50. Thinius, S., Islam, M. M., Heitjans, P. & Bredow, T. Theoretical study of li migration in lithium-graphite intercalation compounds with dispersion-corrected DFT methods. *J. Phys. Chem. C Nanomater. Interfaces* **118**, 2273–2280 (2014).

51. Kobayashi, Y. et al. Direct observation of the ultrafast evolution of Open-Shell biradical in photochromic radical dimer. *J. Am. Chem. Soc.* **139**, 6382–6389 (2017).

52. Amsler, M. et al. Quantum-enhanced quantum monte carlo: an industrial view. Preprint at <http://arxiv.org/abs/2301.11838> (2023).

53. Huggins, W. J., Lee, J., Baek, U., O'Gorman, B. & Birgitta Whaley, K. A non-orthogonal variational quantum eigensolver. *New J. Phys.* **22**, 073009 (2020).

54. Ibe, Y. et al. Calculating transition amplitudes by variational quantum deflation. *Phys. Rev. Res.* **4**, 013173 (2022).

55. Sawaya, N. P. D. & Huh, J. Improved resource-tunable near-term quantum algorithms for transition probabilities, with applications in physics and variational quantum linear algebra. *Adv. Quantum Technol.* **6**, 2300042 (2023).

56. Haghshenas, R., Gray, J., Potter, A. C. & Chan, G. K.-L. Variational power of quantum circuit tensor networks. *Phys. Rev. X* **12**, 011047 (2022).

57. Matthews, D. How to get started in quantum computing. *Nature* **591**, 166–167 (2021).

58. Jiménez-Hoyos, C. A. & Scuseria, G. E. Cluster-based mean-field and perturbative description of strongly correlated fermion systems: Application to the one- and two-dimensional hubbard model. *Phys. Rev. B Condens. Matter* **92**, 085101 (2015).

59. Abraham, V. & Mayhall, N. J. Selected configuration interaction in a basis of cluster state tensor products. *J. Chem. Theory Comput.* **16**, 6098–6113 (2020).

60. Li, Z. Expressibility of comb tensor network states (CTNS) for the p-cluster and the FeMo-cofactor of nitrogenase. *Electron. Struct.* **3**, 014001 (2021).

61. Parker, S. M., Seideman, T., Ratner, M. A. & Shiozaki, T. Communication: Active-space decomposition for molecular dimers. *J. Chem. Phys.* **139**, 021108 (2013).

62. Taube, A. G. & Bartlett, R. J. New perspectives on unitary coupled-cluster theory. *Int. J. Quantum Chem.* **106**, 3393–3401 (2006).

63. Wecker, D., Hastings, M. B. & Troyer, M. Progress towards practical quantum variational algorithms. *Phys. Rev. A* **92**, 042303 (2015).

64. Kandala, A. et al. Hardware-efficient variational quantum eigensolver for small molecules and quantum magnets. *Nature* **549**, 242–246 (2017).

65. Tilly, J. et al. The variational quantum eigensolver: A review of methods and best practices. *Phys. Rep.* **986**, 1–128 (2022).

66. Jordan, P. & Wigner, E. Über das paulische äquivalenzverbot. *Zeitschrift für Physik* **47**, 631–651 (1928).

67. Apaja, V. Quantum monte carlo. <http://users.jyu.fi/~veapaja/QMC/MC-lecture.pdf> (2018).

68. Huang, H.-Y., Kueng, R. & Preskill, J. Predicting many properties of a quantum system from very few measurements. *Nat. Phys.* **16**, 1050–1057 (2020).

69. Zhao, A., Rubin, N. C. & Miyake, A. Fermionic partial tomography via classical shadows. *Phys. Rev. Lett.* **127**, 110504 (2021).

70. Kanno, S., Endo, S., Suzuki, Y. & Tokunaga, Y. Quantum algorithm for the calculation of transition amplitudes in hybrid tensor networks. *Phys. Rev. A* **104**, 042424 (2021).

71. Kiser, M. et al. Classical and quantum cost of measurement strategies for quantum-enhanced auxiliary field quantum monte carlo. Preprint at <http://arxiv.org/abs/2312.09872> (2023).

72. Momma, K. & Izumi, F. VESTA 3 for three-dimensional visualization of crystal, volumetric and morphology data. *J. Appl. Crystallogr.* **44**, 1272–1276 (2011).

Acknowledgements

This work was supported by MEXT Quantum Leap Flagship Program Grants No. JPMXS0118067285 and No. JPMXS0120319794, JSPS KAKENHI Grant No. JP20K05438, and COI-NEXT JST Grant No. JPMJPF2221, and

partly supported by UTokyo Quantum Initiative. A part of this work was performed for Council for Science, Technology and Innovation (CSTI), Cross-ministerial Strategic Innovation Promotion Program (SIP), “Promoting the application of advanced quantum technology platforms to social issues”(Funding agency : QST). The part of calculations were performed on the Mitsubishi Chemical Corporation (MCC) high-performance computer (HPC) system “NAYUTA”, where “NAYUTA” is a nickname for MCC HPC and is not a product or service name of MCC. We acknowledge the use of IBM Quantum services for experiments in this paper. The views expressed are those of the authors, and do not reflect the official policy or position of IBM or the IBM Quantum team. S.K. thanks Kenji Sugisaki and Rei Sakuma for the technical discussion, and Hajime Sugiyama for the technical support on HPC. We would like to thank Editage (www.editage.jp) for English language editing.

Author contributions

S.K. conceived the project and wrote the code for the quantum algorithm. H.N. reviewed the code and analyzed the decomposition for the Heisenberg chain model. H.N., T.N., and S.G. generated the MAB1 Hamiltonian. T.K. provided the structural data for the hydrogen plane models. S.G., M.H., N.Y., and Q.G. provided information for VQE initialization, ansatz selection, Bayesian optimization, and execution on real devices, respectively. All authors discussed the development of the algorithm and analyzed the results. All authors contributed to the writing of the manuscript.

Competing interests

The authors declare no competing interests.

Additional information

Supplementary information The online version contains supplementary material available at <https://doi.org/10.1038/s41534-024-00851-8>.

Correspondence and requests for materials should be addressed to Shu Kanno.

Reprints and permissions information is available at <http://www.nature.com/reprints>

Publisher's note Springer Nature remains neutral with regard to jurisdictional claims in published maps and institutional affiliations.

Open Access This article is licensed under a Creative Commons Attribution 4.0 International License, which permits use, sharing, adaptation, distribution and reproduction in any medium or format, as long as you give appropriate credit to the original author(s) and the source, provide a link to the Creative Commons licence, and indicate if changes were made. The images or other third party material in this article are included in the article's Creative Commons licence, unless indicated otherwise in a credit line to the material. If material is not included in the article's Creative Commons licence and your intended use is not permitted by statutory regulation or exceeds the permitted use, you will need to obtain permission directly from the copyright holder. To view a copy of this licence, visit <http://creativecommons.org/licenses/by/4.0/>.

© The Author(s) 2024